

VHF/UHF detection using high angular momentum Rydberg states

Roger C. Brown,^{1,2,*} Baran Kayim,¹ Michael A. Viray,¹ Abigail R. Perry,^{1,3} Brian C. Sawyer,¹ and Robert Wyllie^{1,†}

¹Georgia Tech Research Institute, Atlanta, Georgia 30332, USA

²NIST 325 Broadway, Boulder, CO 80305

³Quantinuum, 303 S. Technology Ct., Broomfield, CO 80021

(Dated: May 26, 2022)

We demonstrate resonant detection of rf electric fields from 240 MHz to 900 MHz (VHF/UHF) using electromagnetically induced transparency to measure orbital angular momentum $L = 3 \rightarrow L' = 4$ Rydberg transitions. These Rydberg states are accessible with three-photon infrared optical excitation. By resonantly detecting rf in the electrically small regime, these states enable a new class of atomic receivers. We find good agreement between measured spectra and predictions of quantum defect theory for principal quantum numbers $n = 45$ to 70. We utilize data and a numerical model incorporating a five-level master equation solution to estimate the fundamental sensitivity limits of our system.

I. INTRODUCTION

Rydberg atoms have recently been used to measure radio frequency (rf) electric field amplitude [1], polarization [2], phase [3, 4], and angle of arrival [5]. The detected field amplitude is traceable to fundamental atomic structure and has led to a new artifact-free paradigm in rf field calibrations [6–8]. Since the rf field sensing region is defined by laser-atom interaction volume, new opportunities in sub-wavelength rf field visualization have emerged [9, 10]. Temporal modulation of the detected rf field has resulted in communications demonstrations of atomic reception using: amplitude modulation, frequency modulation (AM, FM) [11–15], Binary Phase Shift Keying, and Quadrature Amplitude Modulation [16]. A previous study demonstrated that atomic receivers can operate non-resonantly in the electrically small regime [17]. In this case, the data switching rate was taken to be equal to the carrier frequency (DC to 30 MHz) and not resonant with nearby Rydberg transition frequencies (> 10 GHz). In order for atomic receivers to be compatible with common broadcast technologies (AM/FM radio, television), they must be able to operate with a tunable carrier frequency distinct from the data rate. For example, UHF television channel 17 is centered at 243 MHz with ± 3 MHz of bandwidth. This coincides with the lowest carrier frequencies observed in this paper.

Among the attractive properties of so-called Rydberg receivers is the fact that they are not subject to the Chu limit [18–20] for electrically small antennas. This stems from the difference in the underlying physical mechanism of rf reception between conducting antennas and atoms. The Chu limit states that the bandwidth (BW) is constricted for electrically small passive conductor antennas,

where the characteristic radius of the antenna is less than the wavelength of the rf field, $\ell_{\text{ant}} < \lambda_{\text{rf}}$. Specifically

$$\frac{BW_{\text{Chu}}}{f_0} \lesssim \frac{(2\pi\ell_{\text{ant}})^3}{\lambda_{\text{rf}}^3}, \quad (1)$$

where $f_0 = c/\lambda_{\text{rf}}$ is the carrier frequency and c is the speed of light in vacuum. For example, for a lossless electrically small classical antenna with $2\pi\ell_{\text{ant}}/\lambda_{\text{rf}} = 0.5$, the bandwidth is limited to $BW/f_0 \lesssim 0.1$ [21].

In a typical Rydberg atomic receiver experiment, $f_0 \approx 10$ to 40 GHz, the $BW \lesssim 30$ MHz, and the optical path length in the atomic vapor is $0.5 \text{ cm} < \ell_v < 10 \text{ cm}$ [11–16]. To create an electrically small atomic receiver able to surpass a Chu-limited antenna in the 10 to 40 GHz range, atomic receiver bandwidth will need to be increased about 100-fold while reducing the apparatus size from centimeters to millimeters. However, at reduced carrier frequency, λ_{rf} becomes large such that $\ell_v \ll \lambda_{\text{rf}}$. For example, choosing $f_0 = 300$ MHz with typical atomic parameters ($BW = 10$ MHz, $\ell_v \approx 3 \text{ cm} < \lambda_{\text{rf}} = 1 \text{ m}$) enables an electrically small receiver.

Here, we explore $nF_{7/2} \rightarrow nG_{9/2}$ Rydberg transitions in rubidium vapor with resonances from 240 MHz to 900 MHz for Very High Frequency/Ultra High Frequency (VHF/UHF) rf detection. Two demonstrated approaches to reduce f_0 are: (i) to use non-resonant detection [22–24] and (ii) to increase the principal quantum number, n , of resonant detection [1]. In non-resonant detection schemes, the extension to low rf frequency requires that the amplitude of the detected field be large enough (V/cm to kV/cm) to mix in nearby Rydberg states and often requires the interpretation and simulation of Floquet spectra [22–24]. To maximize sensitivity to incident rf fields, we choose sensors where Autler-Townes (AT) [25] splitting of Rydberg states is resonantly detected with electromagnetically induced transparency (EIT) [26, 27]. This approach senses rf fields with amplitudes below $\mu\text{V}/\text{cm}$ at carrier frequencies defined by the difference in energy between Rydberg states [1]. Reducing f_0 requires optical excitation to higher Rydberg states that are increasingly susceptible

* roger.brown@nist.gov

† robert.wyllie@gtri.gatech.edu

to systematic errors, e.g. DC Stark induced state mixing and long range Rydberg-Rydberg and Rydberg-ground state collisions [28–30]. To our knowledge, the lowest published AT EIT-detected rf signal is at 724 MHz with $n > 130$ [7]. Higher angular momentum ($nF_{7/2} \rightarrow nG_{9/2}$) Rydberg transitions are more than an order of magnitude lower in energetic separation at a given principal quantum number compared to lower angular momentum transitions (see Fig. 3). Using these higher angular momentum states, we demonstrate resonant AT EIT rf sensing with f_0 from 240 MHz to 900 MHz using $n = 75$ to $n = 40$. To achieve $f_0 = 240$ MHz using the more familiar $nP_{3/2} \rightarrow (n-1)D_{5/2}$ transitions would require excitation to $n > 200$.

This paper is structured as follows: In Sec. II we present our experimental apparatus and present measurements of rf transitions between $nF \rightarrow nG$. In Sec. III we present a numerical model and use it to estimate the fundamental noise limits of our data. Finally, in Sec. IV, we conclude with an outlook for future work.

II. EXPERIMENT

To access Rydberg states with orbital angular momentum, $L > 3$, we use the three photon ladder system shown in Figure 1 a. This ladder system has previously been studied in a number of contexts including fundamental atomic structure [31, 32], rf field calibration in the 100 GHz range using both EIT and electromagnetically induced absorption [33], and quantum optics [34]. This ladder system is appealing for a number of reasons. First, all transitions are diode laser accessible. Second, the wavefunction overlaps between successive ladder states are larger than in one- or two-photon Rydberg excitation (increasing Rabi-excitation rates for fixed optical powers). Third, the near degeneracy in optical frequency between the first two steps in optical excitation allows access to nearly all atomic velocity classes [35] [33].

The EIT probe laser beam addresses the $5S_{1/2}, F = 2 \rightarrow 5P_{3/2}, F' = 3$ transition at 780 nm. The effective Rydberg EIT coupling beam is comprised of a two-step optical excitation with a variable intermediate detuning from the $5D_{5/2}, F = 4$ state. The $5P_{3/2}, F = 3 \rightarrow 5D_{5/2}, F' = 4$ transition is at 776 nm, and the $5D_{5/2}, F = 4 \rightarrow nF_{7/2}, F' = 5$ (or $nP_{3/2}, F' = 3$) is tuned from 1260 nm to 1253 nm to access $n = 45$ to $n = 70$ Rydberg states. The intermediate detuning from the $5D_{5/2}$ state can be adjusted to trade Rydberg excitation rate and intermediate-state-lifetime broadening effects.

The optical layout is shown in Figure 1 b. Our rf sensing volume consists of a 75 mm long, 19 mm diameter cylindrical atomic vapor cell with counter-propagating probe and coupling laser beams. The quartz vapor cell is at room temperature, is filled with isotopically pure (98 %) ^{87}Rb , and has fused silica windows at a 2° angle with respect to the laser beam propagation direction.

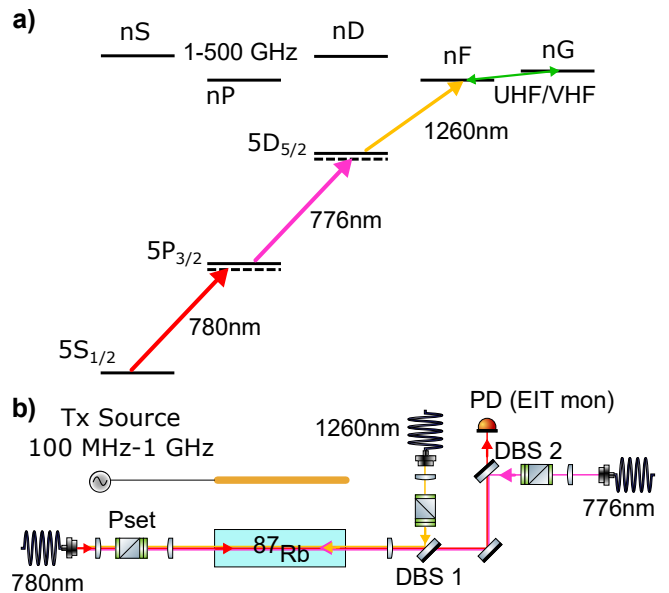


FIG. 1. (a) Level diagram for F -state Rydberg excitation and rf induced Autler-Townes splitting in ^{87}Rb . Three electric dipole-allowed infrared transitions connect the ground state to the Rydberg $nF_{7/2}$ (or $nP_{3/2}$) states. Dashed virtual levels show the single photon detunings of each step from atomic resonance. UHF/VHF fields, depicted with a green bidirectional arrow, can be detected via Autler Townes splitting on the $nF \rightarrow nG$ Rydberg transitions while 1 GHz to 500 GHz can be detected on $nS \rightarrow nP$, $nP \rightarrow (n-1)D$, and $nF \rightarrow (n+1)D$ transitions. (b) Experimental schematic: the 780 nm probe beam counter propagates in a Rb vapor cell with 776 nm and 1260 nm beams which form the effective EIT coupling beam. PD: photodiode; DBS1,2: dichroic beam splitter; Pset: polarization and power control optics consisting of a $\lambda/2$ waveplate and a polarizing beam splitter cube for power control followed by $\lambda/2$ and $\lambda/4$ waveplates for polarization control.

After interacting with the atomic medium, the 780 nm probe beam is dichroically split from the 776 nm and 1260 nm coupling beams and monitored with a photodiode.

The 780 nm, 776 nm, and 1260 nm beam waists ($1/e^2$) are measured to be $55 \mu\text{m}$, $55 \mu\text{m}$, and $65 \mu\text{m}$ with typical powers of $4 \mu\text{W}$, $130 \mu\text{W}$, and 40 mW , respectively. We estimate the upper bounds for optical excitation Rabi rates using the stretched-state dipole matrix elements to be $2\pi \times 30$ MHz for the 780 nm transition, $2\pi \times 55$ MHz for the 776 nm transition, and $2\pi \times 50$ MHz ($2\pi \times 26$ MHz) for the 1260 nm transition to $n = 45$ ($n = 70$) [29]. The 780 nm and 776 nm lasers are frequency stabilized to reference vapor cells using one and two color polarization-rotation spectroscopy [36, 37], respectively. The probe laser is locked 10 MHz below the optical cycling $5S_{1/2}, F = 2 \rightarrow 5P_{3/2}, F = 3$ transition. The intermediate coupling laser is locked 10 to 20 MHz below the $5P_{3/2}, F = 3 \rightarrow 5D_{5/2}, F = 4$ transition. The 1260 nm laser is scanned across the three photon resonance to produce the spectra shown in Figure 2 a.

The 780 nm probe intensity is measured by a photodiode during a scan of the 1260 nm laser frequency across EIT resonance. To calibrate the 1260 nm laser frequency scan, we simultaneously record the transmission of a fiber-based Michelson interferometer with a free spectral range of 33.15(6) MHz, allowing frequency scan non-linearity to be removed in post-processing. The scan center frequency is recorded on a wavemeter with ± 50 MHz accuracy. This wavemeter accuracy is sufficient to identify the principal quantum number of each Rydberg transition; it is not used to measure rf transition frequencies.

The source of rf radiation in our setup is a linear 17 cm monopole antenna connected to an rf synthesizer and placed roughly 20 cm away from the vapor cell. The cell and antenna are mounted 15 cm above an aluminum bread board on a dielectric post. We expect non-trivial contributions from the breadboard to the overall radiation pattern of the antenna since the separation is smaller than the 33 cm to 1.5 m rf wavelengths investigated here.

The EIT line splits into two AT peaks when resonant rf-radiation couples the $nF \rightarrow nG$ transitions. Figure 2 a shows the AT splitting of the $55F \rightarrow 55G$ transition driven by ≈ 3 V/m of 473 MHz as a function of 1260 nm laser detuning in good agreement with a five level optical Bloch equation simulation of the spectrum (see section III for further discussion). Field amplitudes were chosen to generate large peak separation compared to peak widths, not to illustrate minimum resolvable fields. In Figure 2 b we plot the measured Autler-Townes peak frequency splitting of the $60F \rightarrow 60G$ transition as a function of the applied UHF electric field. This shows the expected linear scaling, applicable for use as an rf power standard [1, 7]. The rf electric field can be calculated as:

$$|\vec{E}| = \frac{\hbar}{\mu_R} \Omega_{\text{RF}} \quad (2)$$

using measured AT splitting, Ω_{RF} , and the known transition dipole moment μ_R . We approximate μ_R by assuming a uniform population of Zeeman states and average over the absolute value of all linearly-polarized dipole matrix elements between the sensing Rydberg states.

Figure 3 illustrates the $> 10x$ reduction in carrier frequency (increase in wavelength) at a given n that can be attained by using transitions between higher ($L \geq 3$) angular momentum states. The experimentally measured resonant transition frequencies and uncertainties are shown in green. The measurements are in good agreement with carrier frequencies computed from the ^{85}Rb G -series quantum defect [38–41] after mass scaling [42]. These quantum defect-derived carrier frequencies are shown as solid curves, with the $nF_{7/2} \rightarrow nG_{9/2}$ transitions shown in green. The upper curves on this graph show resonant transition frequencies as a function of n for transitions with lower ($L \leq 3$) orbital angular momenta: $nS_{1/2} \rightarrow nP_{3/2}$, $nP_{3/2} \rightarrow (n-1)D_{5/2}$, and $nF_{7/2} \rightarrow (n+1)D_{5/2}$. These transitions were chosen because they have the largest dipole matrix elements and

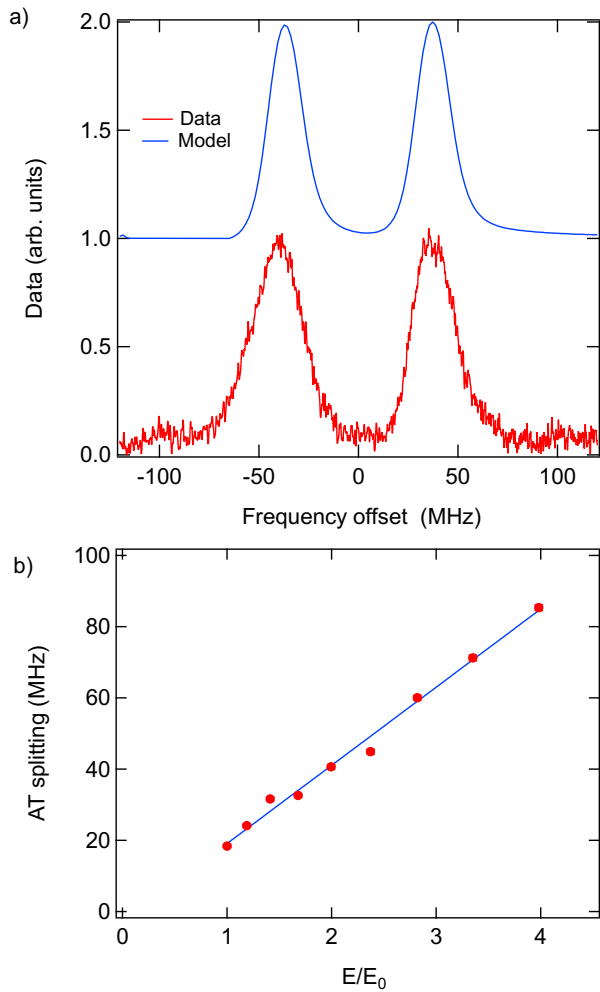


FIG. 2. (a) AT EIT Spectrum of the $55F \rightarrow 55G$ transition with an applied rf field of 473 MHz. A simulated spectrum is offset above the data for clarity. (b) Autler-Townes splitting of the $60F \rightarrow 60G$ EIT signal as a function of applied UHF electric field. This plot confirms the expected linear scaling between rf electric field and Autler-Townes splitting. Uncertainties are smaller than the point markers. $E_0 \approx 0.63$ V/m.

thus are the most sensitive for communications applications.

To determine the resonant Rydberg transition frequency in Fig 3, we record the amplitude and separation of the Autler-Townes peaks as in Fig 2 a. On resonance, the amplitude of the peaks is equal and the separation between the two peaks is minimized. Off of resonance, the peak amplitudes become imbalanced and the peak separation increases. The peak separations as a function of rf frequency reveal an approximately quadratic minimum about the rf carrier frequency. Spectra were recorded in a 30 MHz region approximately centered about the $nF \rightarrow nG$ transition frequency, with a frequency step size of 1 MHz. The peak positions are found by fitting independent Gaussian functions to each Autler-Townes peak. The peak separations are then fit to a quadratic

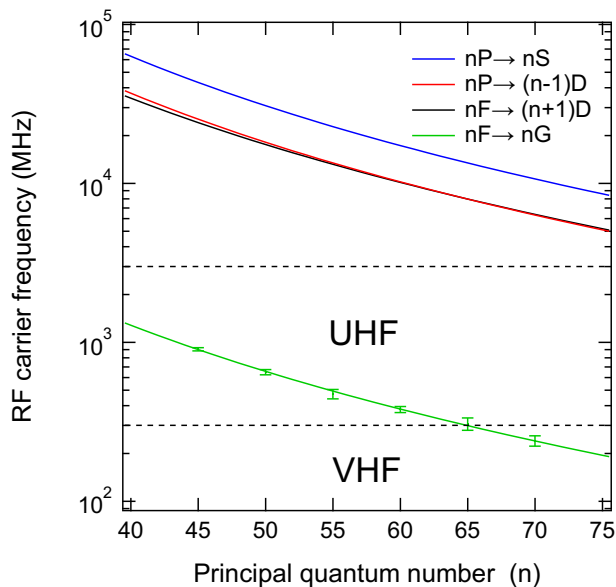


FIG. 3. The red, blue, and black curves show calculated rf carrier frequencies [29] of commonly used lower angular momentum Rydberg states accessible by two photon optical excitation. The green curve is the calculated rf carrier frequency associated with $nF_{7/2} \rightarrow nG_{9/2}$ transitions. The green crosses show corresponding measured carrier frequencies in the $n = 45$ to $n = 70$ range.

to determine Rydberg resonance, with combined fit uncertainties of < 24 MHz on average. We repeat this measurement for several principal quantum numbers in the $n = 45$ to $n = 70$ range.

For this measurement, the vapor cell is more than an order of magnitude smaller than the rf wavelength ($\ell_{\text{vapor}}/\lambda_{\text{rf}} \approx 0.05$). The lowest rf frequency accessible with high angular momentum Rydberg states is not clear. For higher angular momentum transitions the carrier frequencies can be further reduced. For example, the $nG_{9/2} \rightarrow nH_{11/2}$ transitions are a factor of 4.6 lower in frequency at a given principal quantum number than the $nF_{7/2} \rightarrow nG_{9/2}$ transitions. These transitions can be accessed with additional rf fields. When the energetic spacing between transitions approaches the Rabi coupling rate (or potentially data bandwidth in communications applications) between the Rydberg states of interest, the incident rf will couple nearly resonantly to other higher L dipole allowed transitions. This will result in complex spectra not easily interpreted for use in calibration or communication.

III. NUMERICAL MODEL

We develop a numerical model to benchmark our experimental data and compute fundamental sensitivity limits. We use a master equation formalism to simulate the light-atom interaction, as in previous work [33, 43].

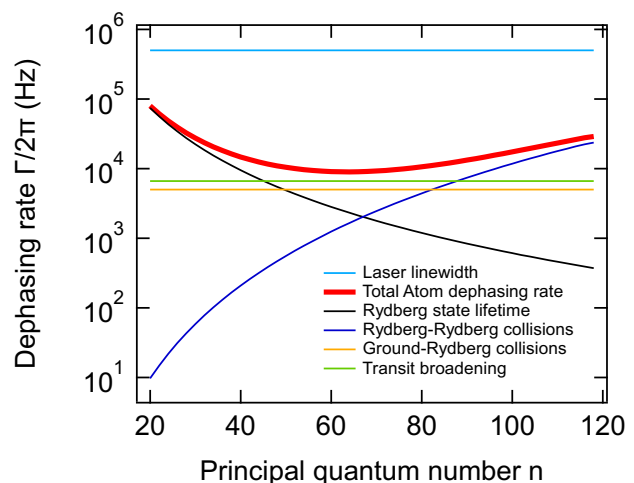


FIG. 4. Dephasing rates versus principal quantum number. Due to competing Rydberg state lifetime and collisional broadening effects, the atom-limited dephasing rate (atom-limited coherence time) is minimized (maximized) at intermediate principal quantum number $40 < n < 80$. This illustrates the advantage of decreasing RF carrier frequency by increasing L rather than increasing n .

We numerically compute the steady-state density matrix for the thermal ^{87}Rb sample. Our numerical model includes the experimental laser beam and rf intensities, propagation directions, polarizations, and frequency detunings from relevant Rb electronic transitions. We account for a number of state decay (T_1) and dephasing (T_2) processes via Lindblad operators [44]. These transition broadening processes include finite laser linewidth, Rb state decay, transit broadening, and electronic-state-dependent collisional broadening (see Fig. 4). We model the system using the five electronic states: $5S_{1/2}$, $5P_{3/2}$, $5D_{5/2}$, $nF_{7/2}$, and $nG_{9/2}$. The steady state is calculated for a range of atom velocities chosen from the Maxwell-Boltzmann distribution.

To account for collision broadening effects, we calculate Van der Waals (C_6) coefficients [45] for both Rydberg-Rydberg ($nF_{7/2}$ - $nF_{7/2}$ and $nF_{7/2}$ - $nG_{9/2}$) and $5S_{1/2}$ -Rydberg atomic collisions. We then use the eikonal approximation with the optical theorem [46] to calculate the total rate Γ_{SR} (Γ_{RR}) for $5S_{1/2}$ -Rydberg (Rydberg-Rydberg) collisions as shown in Fig. 4. We include $5S_{1/2}$ -Rydberg collisional broadening using a phenomenological jump operator of the form $\Gamma_{SR}(|5S_{1/2}\rangle\langle R| + |R\rangle\langle 5S_{1/2}|)$, where $|R\rangle$ is the relevant Rydberg state.

We calculate a transit broadening rate coefficient as the inverse of the average laser beam transit time using a vapor cell temperature $T = 300$ K and the beam waists and generate a corresponding Lindblad operator by summing the outer products of each state vector with the ground state to indicate a T_1 decay. Similarly, we include Lindblad operators for the laser linewidth broadening and the various atomic state lifetimes. The magnitude of each of the aforementioned dephasing rates are repre-

sented in Fig. 4, in addition to a “total atom” dephasing rate, which is the sum of all of the non-laser-dependent atomic broadening effects (collisions and Rydberg state lifetime). The dominant dephasing rate in Fig. 4 is the laser linewidth of the probe distributed Bragg reflector laser. This technical limitation may be overcome by using lasers that are spectrally narrow compared to the natural linewidth of the Rydberg states. Remaining broadening not included in this model may be due to electric field inhomogeneity in the applied RF or nonuniform distribution of metallic rubidium within the vapor cell along the axis of beam propagation. Figure 4 shows two atomic structure limitations to coherence time. At low principal quantum number short atomic lifetimes dominate, while at high principal quantum number Rydberg-Rydberg collisions dominate. The atom-limited dephasing rate (atom-limited coherence time) is therefore minimized (maximized) at intermediate principal quantum number $40 < n < 80$. This optimal atom-limited sensitivity again supports the choice to use $L \geq 3$ states to achieve lower rf carrier frequencies rather than simply going to higher n states.

To compare with absorption measurements, we compute the detuning-dependent optical absorption coefficient (α) experienced by the 780 nm probe laser beam as [33]

$$\alpha = \frac{2k_p n_V \epsilon \mu_p}{\epsilon_0 E_p}, \quad (3)$$

where

$$\epsilon = \int_{-\infty}^{\infty} P(v_x) \text{Im}(\rho_{01}) dv_x \quad (4)$$

is the atomic excitation fraction obtained via integration of the velocity-dependent quantity $\text{Im}(\rho_{01})$ weighted by the Maxwell-Boltzmann velocity distribution along the beam propagation direction, $P(v_x) = \sqrt{\frac{m}{2\pi kT}} \exp(-\frac{mv_x^2}{2kT})$. In Eq. (3), k_p is the probe laser k-vector magnitude, E_p is the probe laser electric field, n_V is the volumetric number density of ^{87}Rb atoms in the cell, μ_p is the electric dipole moment of the $5S_{1/2} \rightarrow 5P_{3/2}$ probe transition, and ϵ_0 is the permittivity of vacuum. Finally, we compute the fractional probe laser beam transmission as $\exp(-\alpha \ell_v)$.

The fundamental sensitivity limits of Rydberg vapor quantum sensors are determined by the quantum projection noise and the photon shot noise [47]. Below, we utilize our model and measurements to estimate the applicable limits to our system in the UHF/VHF frequency ranges investigated here.

The quantum projection noise limited sensitivity to an rf electric field amplitude E_{qpn} is

$$E_{\text{qpn}} = \frac{\hbar}{\mu_R} \frac{1}{\sqrt{NT_2 t}}, \quad (5)$$

for the coherence time T_2 and t is the total measurement time. The number of atoms participating in the measurement is $N = \epsilon n_V V$ for an interaction volume defined by

optical beam geometry $V = \pi w_0^2 \ell_{\text{eff}}$ for beam waists w_0 and effective interaction length ℓ_{eff} . Typical parameters in our simulations yield $10^{-3} < \epsilon < 10^{-2}$, significantly less than an estimation based on all available atoms in the laser beam column [47, 48]. For example, for principal $n = 55$ and the experimental parameters defined above, we estimate $\epsilon = 8 \times 10^{-3}$. If we assume $\ell_{\text{eff}} = 2z_R$ where $z_R = 12$ mm is the Rayleigh range of the probe laser, the corresponding participating atom number is $N \sim 24 \times 10^3$. For the data shown in Figure 2 a, we use the full width at half maximum Γ to estimate $T_2 = \Gamma^{-1}$ [4] and estimate $\Delta E_{\text{qpn}} = 250$ nV/m/ $\sqrt{\text{Hz}}$.

The photon shot noise for a single photodiode intensity measurement is $\Delta I_{\text{psn}} = \sqrt{2e(\eta\epsilon\Phi_p)\Delta f}$, where e is the electron charge, η is the photodiode quantum efficiency, Φ_p is the probe photon flux incident upon the photodiode, and Δf is the measurement bandwidth [49]. Assuming the measurement is made on the side of a peak, the electric field noise will be

$$\begin{aligned} \Delta E_{\text{psn}} &= \Delta I_{\text{psn}} / (\partial I / \partial E) \\ &= \Delta I_{\text{psn}} \frac{2\hbar}{\mu_R} \left(\frac{\partial I}{\partial \omega} \right)^{-1}, \end{aligned} \quad (6)$$

where we have assumed measurement on the side of a single Autler-Townes peak. The factor $\partial I / \partial \omega$ is the slope of the discriminator in photocurrent per angular frequency shift. For the data shown in Figure 2 a, we estimate $\Delta E_{\text{psn}} = 13$ $\mu\text{V}/\text{m}/\sqrt{\text{Hz}}$, a factor of 100 higher than E_{qpn} . To approach these sensitivity limits a number of technical improvements may be made including the addition of: a second probe beam to remove intensity noise, a laser to repump ground state population [50], and a rf local oscillator field to implement super-heterodyne detection [3, 4].

IV. OUTLOOK

We have demonstrated AT-EIT rf field sensitivity on $nF \rightarrow nG$ Rydberg transitions that enable resonant electrically small UHF receivers. Future work includes recording temporally modulated fields to characterize sensitivity and bandwidth at UHF and lower frequencies. This can be done by using portable laser systems and operating in an anechoic chamber, since λ_{rf} is comparable to or larger than many optical elements. Furthermore, this approach is compatible with using auxiliary rf fields to Stark-tune the desired rf frequency [43, 51] offering continuous tuning between atomic transitions.

The three photon all-infrared optical excitation approach also offers a number of benefits that may be further explored. The three optical beams may be aligned in a planar orientation to achieve Doppler-free and recoil-free excitation [52–54] potentially enabling Rydberg lifetime-limited narrow spectral features useful in precise rf field calibrations. Infrared optical excitation may also enable simplified all-dielectric vapor cell sensor

heads with more uniformly applied EIT coupling fields compared to infrared-blue excitation [55]. This should reduce transit broadening and increase sensitivity in a deployable package.

V. ACKNOWLEDGEMENTS

We thank V. Gerginov, R. Westafer, C. D. Herold, and M. Lombardi for comments and careful reading of the manuscript. We acknowledge funding from the Air Force Research Laboratory (AFRL) and the GTRI HIVES program.

-
- [1] J. A. Sedlacek, A. Schwettmann, H. Kübler, R. Löw, T. Pfau, and J. P. Shaffer, Microwave electrometry with Rydberg atoms in a vapour cell using bright atomic resonances, *Nature Physics* **8**, 819 (2012).
- [2] J. A. Sedlacek, A. Schwettmann, H. Kübler, and J. P. Shaffer, Atom-based vector microwave electrometry using rubidium rydberg atoms in a vapor cell, *Phys. Rev. Lett.* **111**, 063001 (2013).
- [3] M. T. Simons, A. H. Haddab, J. A. Gordon, and C. L. Holloway, A Rydberg atom-based mixer: Measuring the phase of a radio frequency wave, *Applied Physics Letters* **114**, 114101 (2019).
- [4] M. Jing, Y. Hu, J. Ma, H. Zhang, L. Zhang, L. Xiao, and S. Jia, Atomic superheterodyne receiver based on microwave-dressed Rydberg spectroscopy, *Nature Physics* **16**, 911 (2020).
- [5] A. K. Robinson, N. Prajapati, D. Senic, M. T. Simons, and C. L. Holloway, Determining the angle-of-arrival of a radio-frequency source with a rydberg atom-based sensor, *Applied Physics Letters* **118**, 114001 (2021).
- [6] E. A. Donley, T. Crowley, T. P. Heavner, and B. Riddle, A quantum-based microwave power measurement performed with a miniature atomic fountain, in *IEEE International Frequency Control Symposium and PDA Exhibition Jointly with the 17th European Frequency and Time Forum, 2003. Proceedings of the 2003* (IEEE, 2003) pp. 135–137.
- [7] C. L. Holloway, M. T. Simons, J. A. Gordon, P. F. Wilson, C. M. Cooke, D. A. Anderson, and G. Raithel, Atom-Based RF Electric Field Metrology: From Self-Calibrated Measurements to Subwavelength and Near-Field Imaging, *IEEE Transactions on Electromagnetic Compatibility* **59**, 717 (2017).
- [8] C. L. Holloway, M. T. Simons, J. A. Gordon, A. Dienstfrey, D. A. Anderson, and G. Raithel, Electric field metrology for si traceability: Systematic measurement uncertainties in electromagnetically induced transparency in atomic vapor, *Journal of Applied Physics* **121**, 233106 (2017).
- [9] H. Q. Fan, S. Kumar, R. Daschner, H. Kübler, and J. P. Shaffer, Subwavelength microwave electric-field imaging using rydberg atoms inside atomic vapor cells, *Opt. Lett.* **39**, 3030 (2014).
- [10] C. L. Holloway, M. T. Simons, M. D. Kautz, A. H. Haddab, J. A. Gordon, and T. P. Crowley, A quantum-based power standard: Using rydberg atoms for a si-traceable radio-frequency power measurement technique in rectangular waveguides, *Applied Physics Letters* **113**, 094101 (2018).
- [11] D. H. Meyer, K. C. Cox, F. K. Fatemi, and P. D. Kunz, Digital communication with Rydberg atoms and amplitude-modulated microwave fields, *Applied Physics Letters* **112**, 211108 (2018).
- [12] Z. Song, H. Liu, X. Liu, W. Zhang, H. Zou, J. Zhang, and J. Qu, Rydberg-atom-based digital communication using a continuously tunable radio-frequency carrier, *Optics Express* **27**, 8848 (2019).
- [13] D. A. Anderson, R. E. Sapiro, and G. Raithel, An atomic receiver for am and fm radio communication, *IEEE Transactions on Antennas and Propagation* **69**, 2455 (2021).
- [14] A. B. Deb and N. Kjærgaard, Radio-over-fiber using an optical antenna based on Rydberg states of atoms, *Applied Physics Letters* **112**, 211106 (2018).
- [15] D. A. Anderson, R. E. Sapiro, and G. Raithel, Rydberg atoms for radio-frequency communications and sensing: Atomic receivers for pulsed rf field and phase detection, *IEEE Aerospace and Electronic Systems Magazine* **35**, 48 (2020).
- [16] C. L. Holloway, M. T. Simons, J. A. Gordon, and D. Novotny, Detecting and receiving phase-modulated signals with a rydberg atom-based receiver, *IEEE Antennas and Wireless Propagation Letters* **18**, 1853 (2019).
- [17] K. C. Cox, D. H. Meyer, F. K. Fatemi, and P. D. Kunz, Quantum-limited atomic receiver in the electrically small regime, *Phys. Rev. Lett.* **121**, 110502 (2018).
- [18] L. J. Chu, Physical limitations of omni-directional antennas, *Journal of Applied Physics* **19**, 1163 (1948).
- [19] H. Wheeler, Fundamental limitations of small antennas, *Proceedings of the IRE* **35**, 1479 (1947).
- [20] R. F. Harrington, Effect of antenna size on gain, bandwidth, and efficiency, *Journal of Research of the National Bureau of Standards-D. Radio Propagation* **64** (1960).
- [21] D. F. Sievenpiper, D. C. Dawson, M. M. Jacob, T. Kanar, S. Kim, J. Long, and R. G. Quarfoth, Experimental Validation of Performance Limits and Design Guidelines for Small Antennas, *IEEE Transactions on Antennas and Propagation* **60**, 8 (2012), conference Name: *IEEE Transactions on Antennas and Propagation*.
- [22] S. A. Miller, D. A. Anderson, and G. Raithel, Radio-frequency-modulated Rydberg states in a vapor cell, *New Journal of Physics* **18**, 053017 (2016).
- [23] Y. Jiao, L. Hao, X. Han, S. Bai, G. Raithel, J. Zhao, and S. Jia, Atom-based radio-frequency field calibration and polarization measurement using cesium nD_J floquet states, *Phys. Rev. Applied* **8**, 014028 (2017).
- [24] E. Paradis, G. Raithel, and D. A. Anderson, Atomic measurements of high-intensity VHF-band radio-frequency fields with a Rydberg vapor-cell detector, *Physical Review A* **100**, 013420 (2019).
- [25] S. H. Autler and C. H. Townes, Stark effect in rapidly varying fields, *Phys. Rev.* **100**, 703 (1955).
- [26] A. K. Mohapatra, T. R. Jackson, and C. S. Adams, Coherent optical detection of highly excited rydberg states

- using electromagnetically induced transparency, Phys. Rev. Lett. **98**, 113003 (2007).
- [27] K.-J. Boller, A. Imamoglu, and S. E. Harris, Observation of electromagnetically induced transparency, Phys. Rev. Lett. **66**, 2593 (1991).
- [28] T. F. Gallagher, *Rydberg Atoms* (Cambridge University Press, Cambridge, 1994).
- [29] N. Šibalić, J. Pritchard, C. Adams, and K. Weatherill, Arc: An open-source library for calculating properties of alkali rydberg atoms, Computer Physics Communications **220**, 319 (2017).
- [30] E. Robertson, N. Šibalić, R. Potvliege, and M. Jones, Arc 3.0: An expanded python toolbox for atomic physics calculations, Computer Physics Communications **261**, 107814 (2021).
- [31] P. Thoumany, T. Germann, T. Hänsch, G. Stania, L. Urbonas, and T. Becker, Spectroscopy of rubidium Rydberg states with three diode lasers, Journal of Modern Optics **56**, 2055 (2009).
- [32] L. A. M. Johnson, H. O. Majeed, B. Sanguinetti, T. Becker, and B. T. H. Varcoe, Absolute frequency measurements of $^{85}\text{Rb } n F_{7/2}$ Rydberg states using purely optical detection, New Journal of Physics **12**, 063028 (2010).
- [33] N. Thaicharoen, K. R. Moore, D. A. Anderson, R. C. Powel, E. Peterson, and G. Raithel, Electromagnetically induced transparency, absorption, and microwave-field sensing in a rb vapor cell with a three-color all-infrared laser system, Phys. Rev. A **100**, 063427 (2019).
- [34] O. Lahad, R. Finkelstein, O. Davidson, O. Michel, E. Poem, and O. Firstenberg, Recovering the Homogeneous Absorption of Inhomogeneous Media, Physical Review Letters **123**, 173203 (2019).
- [35] Access to the largest number of atomic velocity classes occurs when the 780 nm beam counter propagates with the 776 nm and 1260 nm beams and with small frequency offset from $5D_{5/2}$ state, creating stronger spectral features in room temperature atomic vapors than in other three photon excitation schemes.
- [36] C. Wieman and T. W. Hänsch, Doppler-Free Laser Polarization Spectroscopy, Physical Review Letters **36**, 1170 (1976).
- [37] C. Carr, C. S. Adams, and K. J. Weatherill, Polarization spectroscopy of an excited state transition, Optics Letters **37**, 118 (2012).
- [38] J. Han, Y. Jamil, D. V. L. Norum, P. J. Tanner, and T. F. Gallagher, Rb nf quantum defects from millimeter-wave spectroscopy of cold ^{85}Rb rydberg atoms, Phys. Rev. A **74**, 054502 (2006).
- [39] K. Afrousheh, P. Bohlouli-Zanjani, J. A. Petrus, and J. D. D. Martin, Determination of the $^{85}\text{Rb } ng$ -series quantum defect by electric-field-induced resonant energy transfer between cold rydberg atoms, Phys. Rev. A **74**, 062712 (2006).
- [40] L. A. M. Johnson, *Precision laser spectroscopy of rubidium with a Frequency Comb* (University of Leeds, 2011).
- [41] K. Moore, A. Duspayev, R. Cardman, and G. Raithel, Measurement of the rb g -series quantum defect using two-photon microwave spectroscopy, Phys. Rev. A **102**, 062817 (2020).
- [42] The isotope shift between values in ^{85}Rb and the data measured here in ^{87}Rb is accounted for by mass scaling the infinite nuclear mass Rydberg constant $R_\infty = (e^4 m_e)/(16\pi^2 \epsilon_0^2 \hbar^2)$ (here e is the electron charge, m_e is the mass of the electron) by the factor $R_n = R_\infty \times M_n/(M_n + m_e)$ (M_n is the mass of the atomic nucleus) not by adjusting the quantum defects.
- [43] M. T. Simons, A. B. Artusio-Glimpse, C. L. Holloway, E. Imhof, S. R. Jefferts, R. Wyllie, B. C. Sawyer, and T. G. Walker, Continuous radio-frequency electric-field detection through adjacent rydberg resonance tuning, Phys. Rev. A **104**, 032824 (2021).
- [44] D. Manzano, A short introduction to the lindblad master equation, AIP Advances **10**, 025106 (2020).
- [45] H. Q. Fan, S. Kumar, S. Sedlacek, H. Kübler, S. Karimkashi, and J. P. Shaffer, Atom based rf electric field sensing, J. Phys. B: At. Mol. Opt. Phys. **48**, 7 (2015).
- [46] J. J. Sakurai, *Modern quantum mechanics, revised edition*, edited by S. F. Tuan (American Association of Physics Teachers, 1995).
- [47] D. H. Meyer, C. O'Brien, D. P. Fahey, K. C. Cox, and P. D. Kunz, Optimal atomic quantum sensing using electromagnetically-induced-transparency readout, Physical Review A **104**, 043103 (2021).
- [48] D. H. Meyer, Z. A. Castillo, K. C. Cox, and P. D. Kunz, Assessment of Rydberg atoms for wideband electric field sensing, Journal of Physics B: Atomic, Molecular and Optical Physics **53**, 034001 (2020).
- [49] S. Kumar, H. Fan, H. Kübler, A. J. Jahangiri, and J. P. Shaffer, Rydberg-atom based radio-frequency electrometry using frequency modulation spectroscopy in room temperature vapor cells, Optics Express **25**, 8625 (2017), publisher: Optical Society of America.
- [50] N. Prajapati, A. K. Robinson, S. Berweger, M. T. Simons, A. B. Artusio-Glimpse, and C. L. Holloway, Enhancement of electromagnetically induced transparency based rydberg-atom electrometry through population repumping, Applied Physics Letters **119**, 214001 (2021).
- [51] T. Vogt, C. Gross, T. F. Gallagher, and W. Li, Microwave-assisted Rydberg electromagnetically induced transparency, Optics Letters **43**, 1822 (2018).
- [52] G. Grynberg, F. Biraben, M. Bassini, and B. Cagnac, Three-Photon Doppler-Free Spectroscopy: Experimental Evidence, Physical Review Letters **37**, 283 (1976).
- [53] I. I. Ryabtsev, I. I. Beterov, D. B. Tretyakov, V. M. Entin, and E. A. Yakshina, Doppler- and recoil-free laser excitation of rydberg states via three-photon transitions, Phys. Rev. A **84**, 053409 (2011).
- [54] N. Šibalić, J. M. Kondo, C. S. Adams, and K. J. Weatherill, Dressed-state electromagnetically induced transparency for light storage in uniform-phase spin waves, Phys. Rev. A **94**, 033840 (2016).
- [55] M. T. Simons, J. A. Gordon, and C. L. Holloway, Fiber-coupled vapor cell for a portable Rydberg atom-based radio frequency electric field sensor, Applied Optics **57**, 6456 (2018).